RESEARCH ARTICLE

Particle & Particle Systems Characterization
www.particle-journal.com

Synthesis of Gold Nanorod@AuAg Hollow Shell Nanostructures with Enhanced Refractive Index Sensitivity and SERS Activity

Zhen-Ming Shen, Jie Liu, Kun-Peng Wang, Xi-Hao Zhang, Lan Chen, Zhigang Zhou, and Tian-Song Deng**

Hollow core-shell noble metallic nanoparticles have garnered significant attention due to their plasmonic properties, which are markedly enhanced by the hollow structure. However, precisely controlling the size and shape of the shell and cavity in such structures remains a challenge. Here, a novel strategy is reported that eliminates the need for etchants, utilizing monodispersed gold nanorods (AuNRs) as templates to synthesize hollow Au@AuAg core-shell nanostructures. By precisely regulating the CTAB/CTAC and Au/Ag ratios during the co-deposition of Au and Ag atoms onto the AuNRs, uniform bimetallic hollow shells are achieved without the use of corrosive etching agents. High-resolution TEM and EDS characterizations confirm the formation of crystalline AuAg alloy shells surrounding the AuNRs cores, with well-defined cavities. Compared to pure silver shells, the AuAg alloy shells exhibit superior stability. Furthermore, the resulting Au@AuAg nanostructures with hollow shells demonstrate significantly enhanced refractive index sensitivity and surface-enhanced Raman scattering (SERS) activity relative to pristine AuNRs, making them highly promising for biomedical applications such as biosensing and bioimaging.

1. Introduction

Plasmonic nanoparticles have been extensively studied recently due to their excellent optical and electrical properties. These unique properties originate from the strong localized surface plasmon resonance (LSPR) generated on the surface of nanoparticles, which refers to the collective oscillation of conduction electrons at the interface between plasmonic nanoparticles and their surrounding medium when interacting with electromagnetic radiation.[1,2] Among them, gold and silver nanoparticles exhibit broad application potential due to their tunable optical properties in the visible to near-infrared (NIR) range, covering fields such as photoelectronics,[3] catalysis,[4–6] sensing,[7] and therapy.[8]

Numerous studies have shown that the plasmonic properties of gold and silver nanoparticles (NPs) are highly sensitive to their morphology and composition, with different shapes and compositions leading to significant variations in plasmonic characteristics.[9–11] To achieve better performance, researchers have begun to study and synthesize plasmonic nanostructures with complex morphologies and compositions. The demand for multifunctional nanomaterials has driven the emergence of multicomponent core-shell structures. By using existing nanomaterials as the core and coating them with other unique materials in a single or multi-layer shell, whether elemental, composite, or mixed, it has been found that these constructed layers or shells can enable the materials to exhibit functions and properties distinct from those of the isolated core.[12,13] With the formation of the shell layer, the new nanomaterials may display new chemical reactivity or catalytic performance, while the shell structure effectively provides protective functions for the core.[14,15] Such structures provide combined functions from both the core and shell, exhibiting novel properties rather than the single function of individual nanoparticles.[16,17] Additionally, the advent of hollow metal nanoparticles has led researchers to discover that, compared to traditional solid nanomaterials, hollow structures typically exhibit stronger electric fields,[18,19] especially at the shell edges and internal cavity interfaces, making them more sensitive to changes in the refractive index of the surrounding medium. This provides new avenues for enhancing sensing and SERS performance.[20,21] Moreover, the significantly increased surface area-to-volume ratio of hollow metal nanoparticles enables better catalytic activity.[22,23] Combining hollow and core-shell structures results in a configuration known as a rattle-type or yolk–shell structure.[24,25] This design integrates the solid properties of the inner core and outer shell with the characteristics of the cavity between them.[18,26] In recent years, such multifunctional nanomaterials have attracted considerable attention and have shown

Z.-M. Shen, J. Liu, K.-P. Wang, X.-H. Zhang, L. Chen, Z. Zhou, T.-S. Deng
School of Electronics and Information Engineering
Hangzhou Dianzi University
Hangzhou 310018, China
E-mail: liujie4209@hdu.edu.cn; dengts@pku.edu.cn
T.-S. Deng
Key Laboratory of Micro-nano Sensing and IoT of Wenzhou
Wenzhou Institute of Hangzhou Dianzi University
Wenzhou 325038, China

The ORCID identification number(s) for the author(s) of this article can be found under https://doi.org/10.1002/ppsc.202500110

DOI: 10.1002/ppsc.202500110

promising applications as sensors, nanoreactors, drug/gene delivery carriers, and lithium-ion battery components.[27–30]

Presently, the preparation of hollow core-shell nanostructures mainly involves five methods: selective etching, soft template assembly, ship-in-bottle, Ostwald ripening, and galvanic replacement.[24] Selective etching entails coating the core nanoparticles with two layers of different materials and then selectively etching the intermediate layer using appropriate solvents or calcination steps to achieve a hollow structure.[31,32] The soft template assembly method uses soft templates (fluorocarbon surfactants or mixed surfactant aggregates) to capture or encapsulate the core nanoparticles, followed by sol-gel reactions of silica sources around the periphery of the soft templates to form hollow silica or PMO shells.[33,34] The ship-in-bottle approach involves prefabricating a hollow cavity structure, then allowing precursors of the core material to diffuse into the cavity through channels, where they form or immobilize solid core particles through chemical reactions or physical encapsulation, resulting in the desired core-shell hollow structure.[35,36] Ostwald ripening is a physical method that involves the growth of smaller crystals into larger ones, during which the core is coated to form a hollow core-shell structure.[37,38] Galvanic replacement involves replacing the metal template of the nanostructure with another less active metal, offering a simple and effective construction method.[25,39] Despite these effective methods, precisely controlling the size and shape of the shell and hollow cavity remains a challenge.

In this study, gold nanorods (AuNRs) are selected as the core, and a hollow structure of gold-silver alloy shell is formed by simultaneously growing gold and silver atoms on the surface of the AuNRs. This Au@AuAg hollow shell structure is different from previously reported Au@AuAg structures and does not involve corrosion to create the hollow structure. We systematically investigated the plasmonic properties of Au@AuAg. It is found that compared to AuNRs, Au@AuAg exhibits higher refractive index sensitivity and superior surface-enhanced Raman scattering (SERS) activity. Additionally, we compared the stability of Au@AuAg with that of Au@Ag with a pure silver shell. Due to the presence of the gold-silver alloy shell, Au@AuAg demonstrated better stability.

2. Results and Discussion

In this study, AuNRs are chosen as the plasmonic core material because their LSPR can be easily tuned by adjusting the aspect ratio (length/diameter), and their spectral range varies from 600 to over 1200 nanometers, which coincides with the region where sunlight is most intense.[40] We prepared AuNRs using a seed-mediated growth method with slight modifications[41] (see Experimental Section). The prepared AuNRs exhibited a length of 90.8 ± 6.8 nm and width of 18.4 ± 2.1 nm (Figure S1b, Supporting Information), and their UV–vis–NIR absorption spectra are shown in Figure S1a (Supporting Information). The extinction spectrum of the AuNRs display longitudinal LSPR at 890 nm and transverse LSPR at 508 nm. By individually introducing $HAuCl_4$ and $AgNO_3$ into the AuNRs solution followed by addition of ascorbic acid (AA), we achieved growth of Au@Au nanostructures and core-shell structures with silver shells (Au@Ag). Simultaneously introducing hydrogen tetrachloroaurate ($HAuCl_4$) and silver nitrate ($AgNO_3$) into the gold nanorod solution, a gold-silver hollow core-shell structure (Au@AuAg) can be fabricated by fine-tuning the amounts of $HAuCl_4$ and $AgNO_3$ (**Scheme 1**). During synthesis, glycine and sodium hydroxide are employed for pH adjustment. Previous studies have demonstrated that pH significantly affects the growth of gold and silver; optimizing the pH to 8.5 facilitated simultaneous rapid growth of both metals.[42] The UV–vis–NIR extinction spectra of the Au@Ag and Au@Au structures are shown in Figure S2a (Supporting Information). The longitudinal LSPR peak of Au@Ag is located at 683 nm, exhibiting a blueshift of 192 nm compared to the original AuNRs. Transmission electron microscopy (TEM) images revealed that the aspect ratio of Au@Ag decreased to 3.03 from the initial 4.93 of the AuNRs (Figure S2b, Supporting Information). Notably, the distinct core-shell morphology observed in TEM images and the transverse LSPR signal at wavelengths below 500 nm confirmed successful growth of the silver shell. For Au@Au, the longitudinal LSPR peak shifted to 820 nm, corresponding to a blueshift of 70 nm relative to the AuNRs. TEM characterization of Au@Au demonstrated irregular end structures and peripheral protrusions on the AuNRs after secondary growth, attributed to rapid gold atom deposition under high-pH conditions, resulting in kinetically controlled geometric configurations.[42] Additionally, its aspect ratio is measured to be 3.49, exhibiting a reduction from 4.93 compared to the pristine AuNRs (Figure S2c, Supporting Information).

We experimentally observed that the ratio of $HAuCl_4$ to $AgNO_3$ significantly influences the growth of hollow shells. To investigate the impact of the $HAuCl_4$ and $AgNO_3$ precursors on the final nanostructures, experiments wer conducted by varying the $HAuCl_4/AgNO_3$ ratio while maintaining a constant total precursor concentration of 0.28 mM. UV–vis–NIR spectra and the corresponding TEM images are presented in **Figures 1a–f** and S3 (Supporting Information). As the proportion of $HAuCl_4$ increased, the hollow shell structure became progressively more distinct. This hollowing effect initially manifested at both ends of the nanostructures (Figure 1b; Figure S3a, Supporting Information), subsequently extending laterally (Figure 1c; Figure S3b, Supporting Information). When the proportion of $HAuCl_4$ reached 30%, we obtained a uniformly hollow shell structure (Figure 1d; Figure S3c, Supporting Information). However, upon further increasing the $HAuCl_4$ proportion, the hollow shell structure rapidly diminished. When the $HAuCl_4$ proportion reached 50%, the hollow structure had largely disappeared; consequently, higher proportions were not explored. Figure 1a illustrates the evolution of the UV–vis–NIR spectra of Au@AuAg nanoparticles with increasing $HAuCl_4$ proportion. For $HAuCl_4$ proportions below 30%, the longitudinal LSPR peak exhibited a redshift accompanied by a gradual decrease in intensity as the $HAuCl_4$ proportion increased. In contrast, for $HAuCl_4$ proportions exceeding 30%, the spectral trend reversed: the longitudinal LSPR peak underwent a blueshift, and its intensity progressively increased. This shift reversal arises from the competing effects of free electron density and interband transition damping. At Au proportions below 30% (corresponding to higher Ag content), the free electron density dominates. Silver possesses a higher free electron density than gold. Since free electron density governs the plasmonic oscillation frequency, a reduction in this density lowers the plasmonic frequency, resulting in the LSPR redshift. When the Au

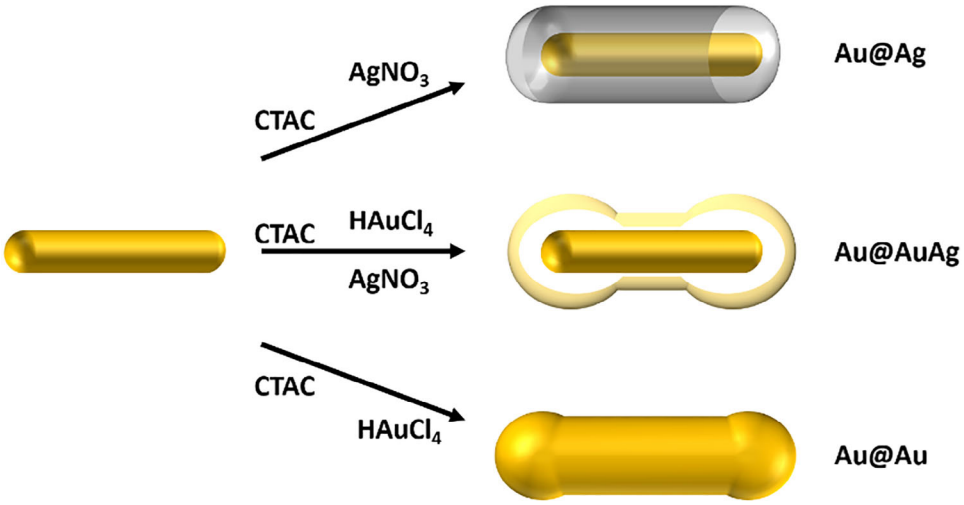

Scheme 1. Schematic illustration of the synthesis process for different core-shell structures.

proportion exceeds 30%, interband transition damping becomes the dominant factor. Silver exhibits weaker interband damping compared to gold. The increasing gold proportion enhances interband damping, which restricts the collective oscillation amplitude of the free electrons, thereby inducing the LSPR blueshift. Notably, this trend in LSPR behavior parallels the evolution of the hollow shell structure, suggesting a correlation between the LSPR shifts and the formation of the hollow nanostructure. Morphological analysis revealed that the Au@AuAg hollow shells exhibited an external length of 113.2 ± 9.1 nm and an external width of 43.2 ± 3.3 nm (Figure S4a,c, Supporting Information). The internal hollow cavity measured 98.6 ± 7.1 nm in length and 29.6 ± 2.9 nm in width (Figure S4b,d, Supporting Information). To elucidate the elemental distribution and crystal structure of the Au@AuAg nanostructures, high-resolution transmission electron microscopy (HRTEM) and EDS elemental mapping are performed (Figure 1g,h). The HRTEM image (Figure 1g) revealed lattice fringes within the hollow shell with a measured spacing of 2.07 Å, corresponding to the Au {200} planes. In the EDS images (Figure 1h), gold and silver are represented by yellow and green, respectively. The images indicate a homogeneous distribution of both Au and Ag within the hollow shell, except for a gold-rich core region attributed to the initial gold nanorod template. This uniformity confirms the formation of an AuAg alloy shell. To quantitatively verify the elemental composition of the AuAg alloy shell, EDS analysis is specifically conducted on the edge region of a hollow shell, deliberately avoiding the gold nanorod core (Figure S5a, Supporting Information). The net counts from the EDS spectrum (Figure S5b, Supporting Information) yielded a composition of 37.07% Au and 62.93% Ag for the hollow shell. This measured ratio is close to the nominal 30% Au proportion used in the synthesis, demonstrating that pH adjustment enabled precise control over the Au/Ag ratio in the final hollow shell structure.

In previous studies, when CTAB was used as a surfactant and the pH was maintained at 8.5 during the simultaneous growth of gold and silver on AuNRs, nano-shuttle structures were formed instead of hollow structures.[43] To investigate the effect of CTAB and CTAC surfactants on the formation of hollow structures, we adjusted the ratio of CTAB to CTAC while maintaining a constant Au/Ag ratio of 30%. Spectral analysis revealed that as the CTAC proportion decreased, the longitudinal LSPR exhibited a redshift, and the absorbance in the 400–600 nm range gradually increased (**Figure 2a**). Corresponding TEM characterization (Figure 2b–e; Figure S6, Supporting Information) showed that reducing CTAC content induced the gradual formation of sharp protrusions at both ends of the AuNRs, ultimately leading to nano-shuttle structures. Notably, when the CTAC ratio is ≥75%, the system still maintained a hollow structure; however, when the CTAC ratio dropped below 50%, the hollow structure completely disappeared, transitioning to a uniform core-shell structure. These phenomena are closely related to crystal growth kinetics. Previous studies have shown that in CTAB-dominated systems, Au^{3+}/Ag^{+} preferentially grow anisotropically along the {100} and {111} facets, with the preferential growth of the {111} facet directly leading to the formation of shuttle-shaped tips.[26,44] In CTAC-dominated systems, ions preferentially adsorb on the {100} facets of the sides, driving longitudinal anisotropic growth. This explains the suppression of tip formation and the preferential hollow structure formation at both ends under high CTAC content. The formation of the hollow shell involves a displacement reaction. The reduction potential of Au^{3+}/Au (+1.50 V) is significantly higher than that of $\frac{Au^{+}}{Ag}$ (+0.80 V), leading to the spontaneous oxidation of Ag by Au^{3+} and the deposition of Au. The overall reaction process is as follows:

$$3Ag + AuCl_4^- \rightarrow Au + 3Ag^+ + 4Cl^- \quad (1)$$

Under the reduction of excess ascorbic acid (AA), Ag^+, with its lower reduction potential, is preferentially reduced to atoms and deposited onto the gold nanorods. However, as the reaction proceeds, both Au^{3+} and Ag^+ are reduced simultaneously, and the initially formed Ag layer is consumed through a displacement reaction, leading to the formation of the hollow layer. In CTAB-dominated systems, the rapid deposition of Au^{3+}/Ag^+ on the {111} facets results in a defect-free, continuous shell layer. The high compactness of this shell structure inhibits the

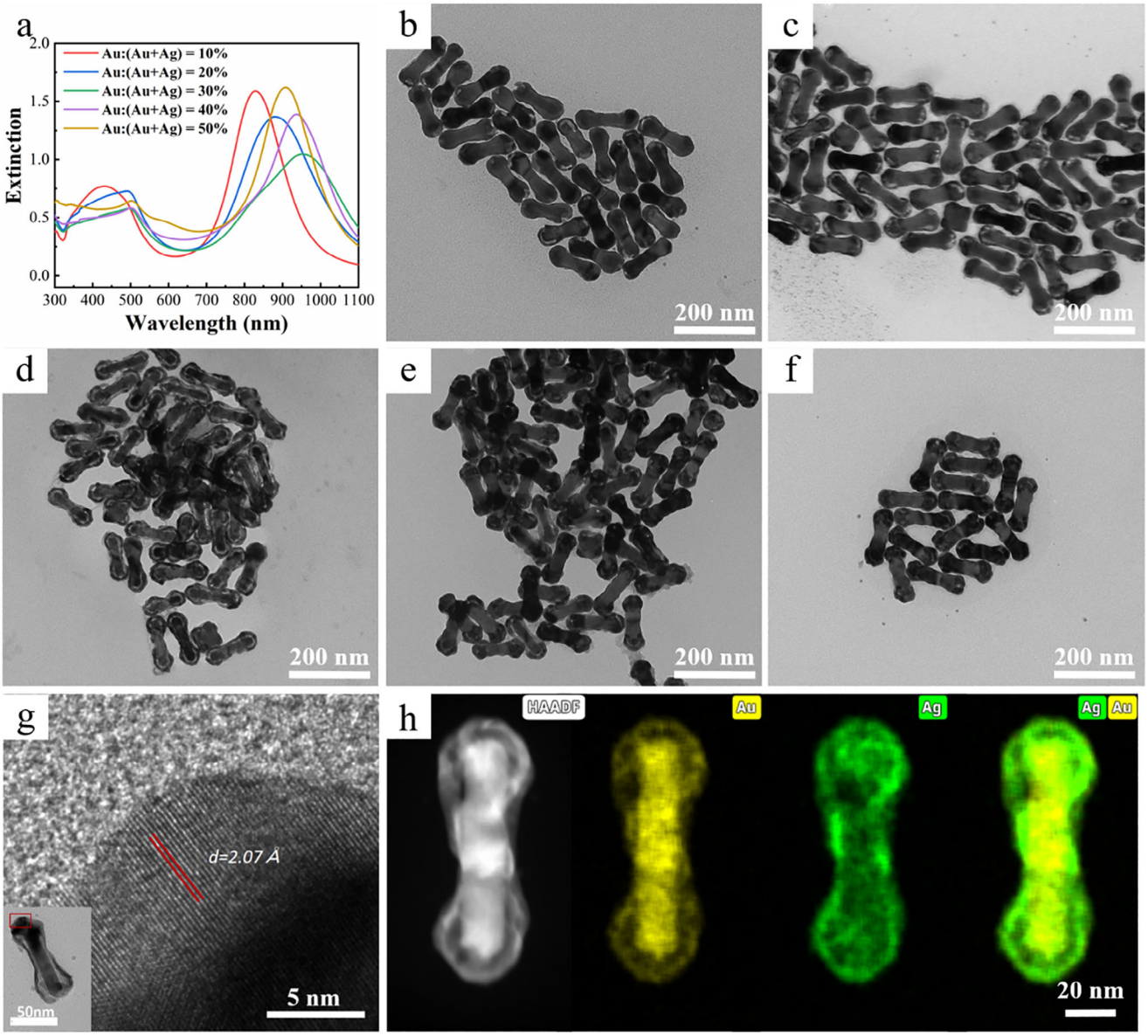

Figure 1. Morphological control of Au@AuAg nanostructures by adjusting the precursor ratio of $HAuCl_4/(HAuCl_4 + AgNO_3)$. a) UV–vis–NIR spectra of Au@AuAg with varying $HAuCl_4/ (HAuCl_4 + AgNO_3)$ ratios. b–f) TEM images of Au@AuAg synthesized at different precursor ratios: b) 10%, c) 20%, d) 30%, e) 40%, and f) 50%. g) HRTEM image of Au@AuAg with a 30% $HAuCl_4$: $(HAuCl_4 + AgNO_3)$ ratio. h) HAADF-STEM images and Elemental EDS mapping of Au@AuAg with a 30% $HAuCl_4$: $(HAuCl_4 + AgNO_3)$ ratio.

displacement reaction, giving rise to a uniform AuAg alloy shell. In contrast, in CTAC-dominated systems, the growth of Au^{3+}/Ag^{+} along the {110} end facets creates an open structure, allowing the displacement reaction to occur and facilitating the formation of the hollow layer. This explains why the hollow layer emerges as the CTAC concentration decreases.

To investigate the refractive index sensitivity of the plasmon resonance peaks of Au@AuAg hollow core-shell structures, they were dispersed in binary mixtures of water and glycerol, with the volume percentage of glycerol varied. For comparison, AuNRs with a longitudinal LSPR at 958 nm, close to that of Au@AuAg, were selected as a control to compare refractive index sensitivity. In all experiments, the maximum volume percentage of glycerol is 73.63%. As the refractive index of the solvent mixture increased, the transverse LSPR exhibited a redshift (**Figure 3**a,b). The transverse LSPR peaks of Au@AuAg also showed a redshift with increasing refractive index, whereas the transverse LSPR of AuNRs remained nearly unchanged (Figure 3d,e). The peak wavelengths in different solvents were measured, and the plasmon shift is determined by the difference between the peak wavelengths in the solvent mixture and pure water. The refractive index of the solvent mixture is calculated using the Lorentz equation. When plotting the plasmon shift as a function of the refractive index of the solvent mixture, both longitudinal and transverse LSPR exhibited approximately linear relationships. All curves were well-fitted by linear approximations, and the slopes of these

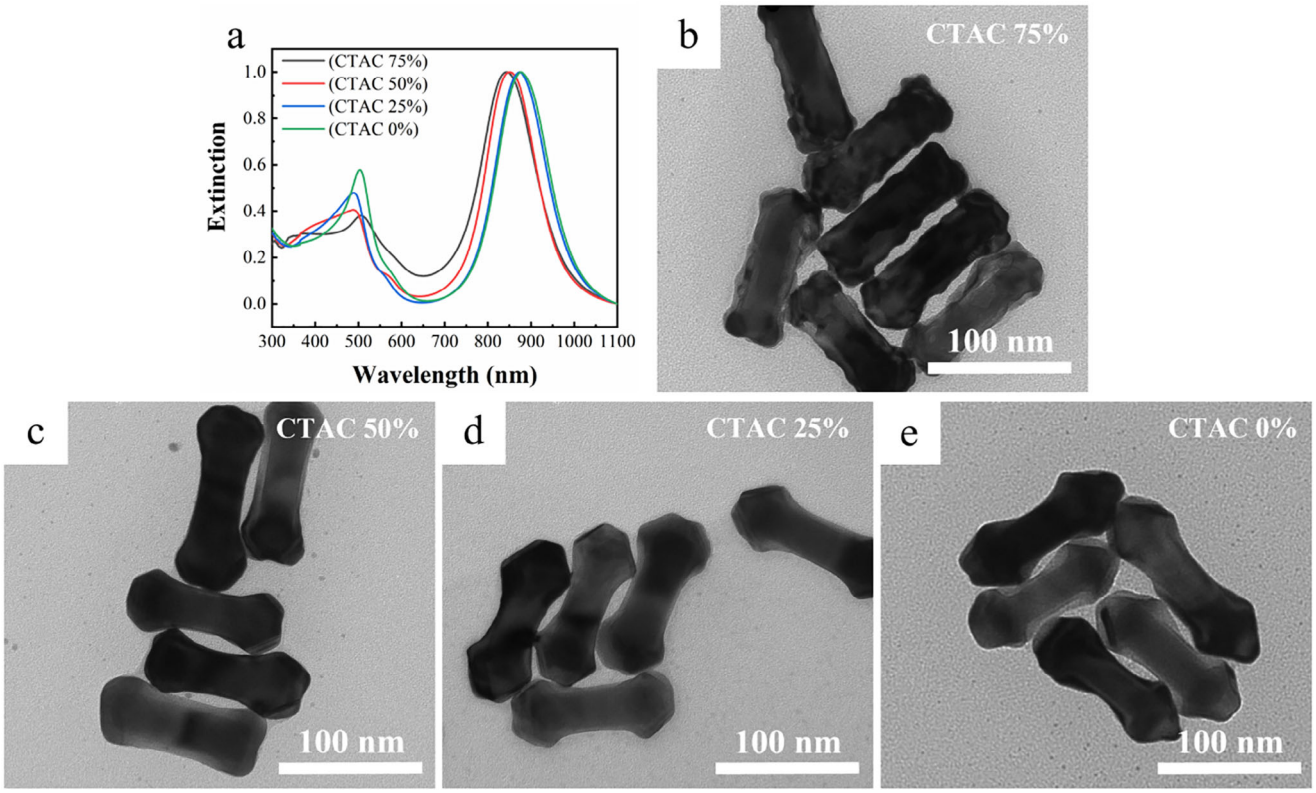

Figure 2. Morphological control of Au@AuAg nanostructures by adjusting the surfactant ratio of CTAC/(CTAB + CTAC). a) UV–vis–NIR spectra of Au@AuAg at different CTAC/(CTAB + CTAC) ratios. b–e) TEM images of Au@AuAg synthesized at different surfactant ratios: b) 75%, c) 50%, d) 25%, e) 0%.

lines represented the refractive index sensitivity (Figure 3c,f). The values are summarized in **Table 1**. From Figure 3c,f and Table 1, it is evident that the refractive index sensitivity of Au@AuAg is significantly higher than that of AuNRs. This demonstrates that the hollow core-shell structure enhances the refractive index sensitivity of the plasmon resonance peaks.

To investigate the surface-enhanced Raman scattering (SERS) effect of Au@AuAg and AuNRs, we conducted SERS tests on the two nanomaterials separately. The Au@AuAg nanoparticles possess a hollow structure and contain a significant amount of silver in their alloy shell. According to theoretical and experimental studies, silver nanoparticles exhibit higher SERS activity than gold nanoparticles. Therefore, it is expected that Au@AuAg nanoparticles would produce greater SERS enhancement. In Raman sensing applications, Au@AuAg should be more advantageous than AuNRs due to its superior SERS enhancement. To verify the universality of Au@AuAg SERS enhancement, we selected two dyes for SERS testing: methylene blue (MB) and crystal violet (CV) (**Figure** 4a,b). Figure 4a shows the SERS spectrum of CV, where the absorption peak at 802 cm^{-1} corresponds to the bending vibration of phenyl-H, the peak at 913 cm^{-1} originates from the ring skeleton vibration, the peak at 1173 cm^{-1} is attributed to the ring C—H bending vibration, the peak at 1385 cm^{-1} corresponds to the stretching vibration of CV, and the peak at 1614 cm^{-1} is attributed to the C—C ring stretching vibration of CV.[45,46] Figure S7a (Supporting Information) presents the intensity of AuNRs and Au@AuAg at the five characteristic peaks of CV. We observed that regardless of the characteristic peak, Au@AuAg consistently exhibited stronger SERS enhancement than AuNRs. Figure 4b shows the SERS spectrum of MB, which detects five distinct characteristic peaks of MB at 440, 799, 1176, 1371, and 1620 cm^{-1}. These peaks correspond to the skeletal bending vibration of C—N—C, the in-plane bending vibration of C—H, the stretching vibration of C—N, the planar ring deformation vibration of C—H, and the stretching vibration of the C—C ring, respectively.[47–49] Figure S7b (Supporting Information) shows the intensity of AuNRs and Au@AuAg at the five characteristic peaks of MB. Similar to CV, the SERS enhancement effect of Au@AuAg is significantly higher than that of AuNRs. To quantitatively evaluate the performance advantage of the SERS, we calculated the enhancement factor (EF) for the two dyes at their respective characteristic peaks using the following formula:[50]

$$EF = \frac{I_S}{I_R} \cdot \frac{N_R}{N_S} \quad (2)$$

Where I_S and I_R represent the relative intensities of the characteristic peak in the SERS spectrum and the pure dye Raman spectrum, respectively. $N_S$and N_R denote the concentrations of dye adsorbed on the SERS substrate and the conventional Raman substrate, respectively. Figure S8 (Supporting Information) displays the EF of AuNRs and Au@AuAg nanostructures at various characteristic peaks for different dyes. When CV is

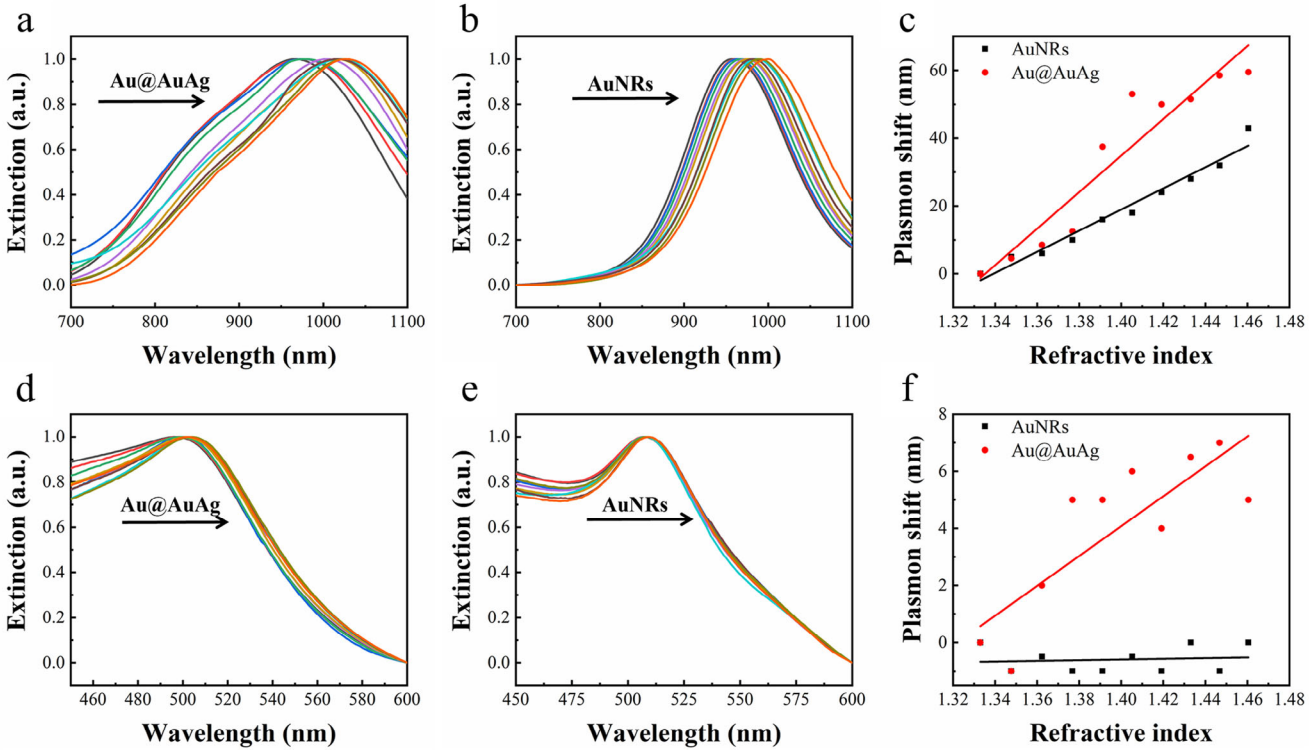

Figure 3. Longitudinal LSPR (a: Au@AuAg, b: AuNRs) and transverse LSPR (d: Au@AuAg, e: AuNRs) of extinction spectra in water-glycerol mixtures with different compositions. Each extinction spectrum is normalized to its maximum intensity. The arrows indicate the direction of increasing glycerol volume percentage. Figure 3c shows the longitudinal LSPR shift for AuNRs and Au@AuAg, and Figure 3f shows the relationship between the transverse LSPR shift and the refractive index of the liquid mixture.

employed as the dye, all EF values for Au@AuAg exceeded 40, with the maximum value of 145 observed at 1385 cm^{-1}. Comparative analysis with AuNRs at corresponding peaks reveals that their EF values are significantly lower, and consistently showing Au@AuAg exhibited approximately fivefold higher enhancement across all tested peaks (Figure S8a, Supporting Information). Analogous results are obtained using MB as the dye: all EF values for Au@AuAg surpassed 116, representing roughly four times greater enhancement than AuNRs (Figure S8a, Supporting Information). These quantitative comparisons validate the remarkable SERS improvement achieved by the Au@AuAg over pristine AuNRs.

The primary mechanism for Raman enhancement is the interaction between light and the free electrons on the metal surface, which induces electronic oscillations, known as the plasmonic effect. This effect amplifies the electromagnetic field around the metal, and the enhanced electromagnetic field interacts with the analyte molecules adsorbed on the metal surface, leading to a substantial increase in the Raman signal.[51] To investigate the electric field distribution of the sample particles at a wavelength of 633 nm, we performed finite-difference time-domain (FDTD) simulations on Au@AuAg and obtained the extinction spectrum and electric field distribution of a single Au@AuAg nanostructure (Figure 4c,d). Figure 4c shows the simulated extinction spectrum (solid line), which is in good agreement with the experimental results (dashed line). The broadening of the peaks in the experimental spectrum can be attributed to factors such as the polydispersity of the nanostructures and shell thickness. The consistency between the simulated and experimental spectra validates the accuracy of our simulations. Figure 4d presents the electric field distribution of a single Au@AuAg nanostructure at a wavelength of 633 nm. The Au@AuAg nanostructure exhibits significant electric field enhancement at the hollow positions on both sides of the sample and at the tips of the internal gold nanorod.

Furthermore, we investigated the influence of varying Au/(Au+Ag) ratios in the alloy shell of Au@AuAg structures on their electric field distribution (Figure S9, Supporting Information). As gold content increases, the localized near-field intensity exhibits a non-monotonic trend—initially decreasing before subsequently increasing. Irrespective of composition, significant field enhancement consistently occurs at both hollow side regions and particle termini. Based on this phenomenon, we analyzed the electromagnetic enhancement mechanism in Au@AuAg systems: fundamentally driven by incident light

Table 1. The refractive index sensitivity of AuNRs and Au@AuAg hollow shell structures.

Samples	λ_T [nm]	λ_L [nm]	Index sensitivity of transverse LSPR [nm/RIU]	Index sensitivity of longitudinal LSPR [nm/RIU]
AuNRs	508	958	1.2	311.9
Au@AuAg	497	966.5	52.3	538.7

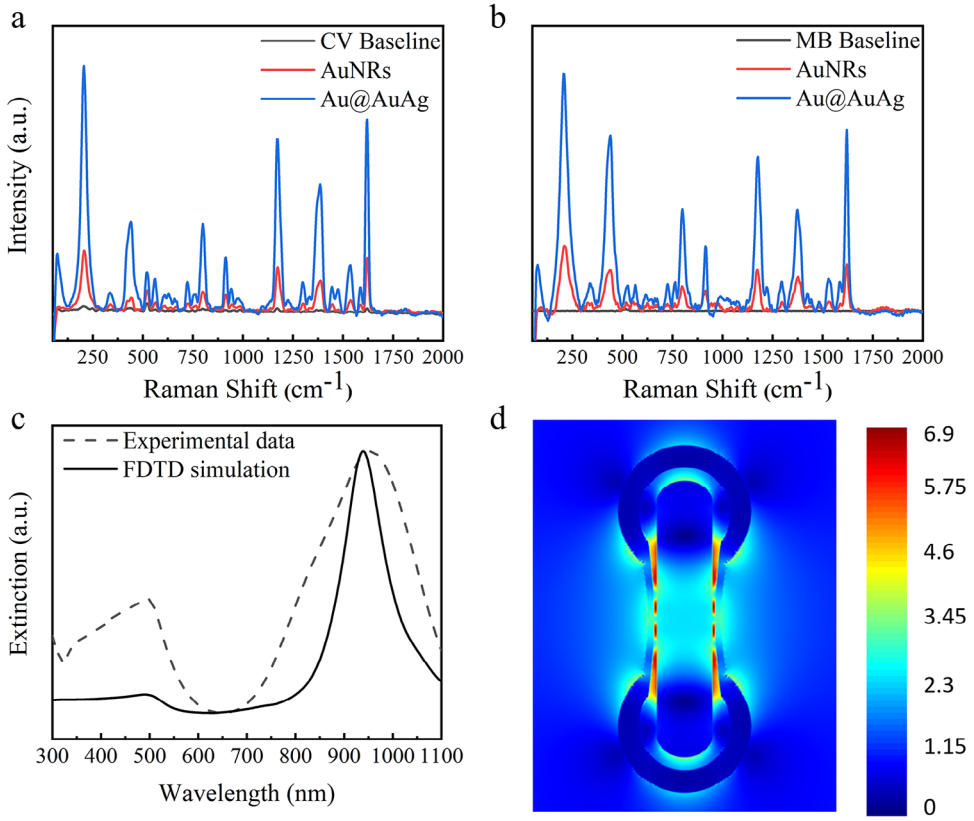

Figure 4. SERS tests and FDTD simulations of AuNRs and Au@AuAg hollow structures. a) SERS spectra of CV. b) SERS spectra of MB. c) Simulated (solid line) and experimental (dashed line) spectra of a single Au@AuAg nanostructure. The size parameters of the Au@AuAg in the simulation are derived from experimental data, with an outer length of 113 nm, outer width of 43 nm, inner length of 98 nm, inner width of 29 nm, and internal AuNRs dimensions of 90.8 nm in length and 18.4 nm in width. By setting the polarization direction parallel to the long axis of the nanostructure (Y-axis in d), only the longitudinal LSPR is calculated. d) Electric field distribution of a single Au@AuAg nanostructure.

interacting with free electrons on LSPR, which amplifies surrounding electromagnetic fields. Specifically, the high curvature at particle tips facilitates the formation of hotspots marked by intense electric fields. Simultaneously, the nanoscale gap between core and shell enables strong coupling between their respective LSPR, resulting in hybridized modes that generate substantially magnified localized fields. The observed non-monotonic behavior arises from the interplay between two competing factors: the dominant LSPR contribution from silver compared to gold, and the increasingly influential effect of strong coupling. When silver dominates the shell, significant dielectric mismatch with the core impedes efficient coupling, causing the system to rely predominantly on silver's intrinsic LSPR effect; consequently, increasing the gold fraction reduces the overall field strength. Conversely, when the shell has a higher gold composition, its permittivity approaches that of the Au core, dramatically enhancing core-shell coupling. This strengthened interaction reinforces electric fields bilaterally. In this regime, the strong coupling effect prevails, counteracting the reduction in LSPR strength due to lower silver content, ultimately leading to renewed field enhancement as gold content increases.

To investigate the stability of the obtained hollow nanostructures, we conducted a corrosion experiment using Au@Ag as a control (**Figure 5**). Figure 5a shows the UV–vis–NIR spectral analysis, which indicates that the Au@Ag core-shell structure undergoes rapid corrosion in a mixed solvent system of hydrogen peroxide (H_2O_2) and ammonia ($NH_3{\cdot}H_2O$). The characteristic spectrum quickly evolves toward that of AuNRs, and the solution color changes abruptly from green to a brownish-pink color, similar to that of an AuNRs solution, confirming the complete corrosion of the silver shell. Figure 5b presents the dynamic UV–vis–NIR spectral changes of the Au@AuAg alloy structure. During the reaction, the volatilization of ammonia caused slight spikes in the spectrum, but compared to the pure silver shell system, the stability of Au@AuAg in the etchant is significantly improved, with only a slow decay in the intensity of its characteristic peaks. Figure 5c further quantifies the decay rate of the absorption peak intensity of Au@AuAg over time. The data show that the decay rate of the absorption peak intensity gradually slows down and stabilizes as the reaction proceeds. After 2 h, the intensity retention rate reaches 85.9%, and there is no significant change in the solution color (Figure 5b), fully demonstrating the excellent stability of the gold-silver alloy shell. Prior studies have also shown that, compared to pure silver structures, gold-silver alloy structures can significantly enhance the chemical stability of nanomaterials in corrosive environments.[52]

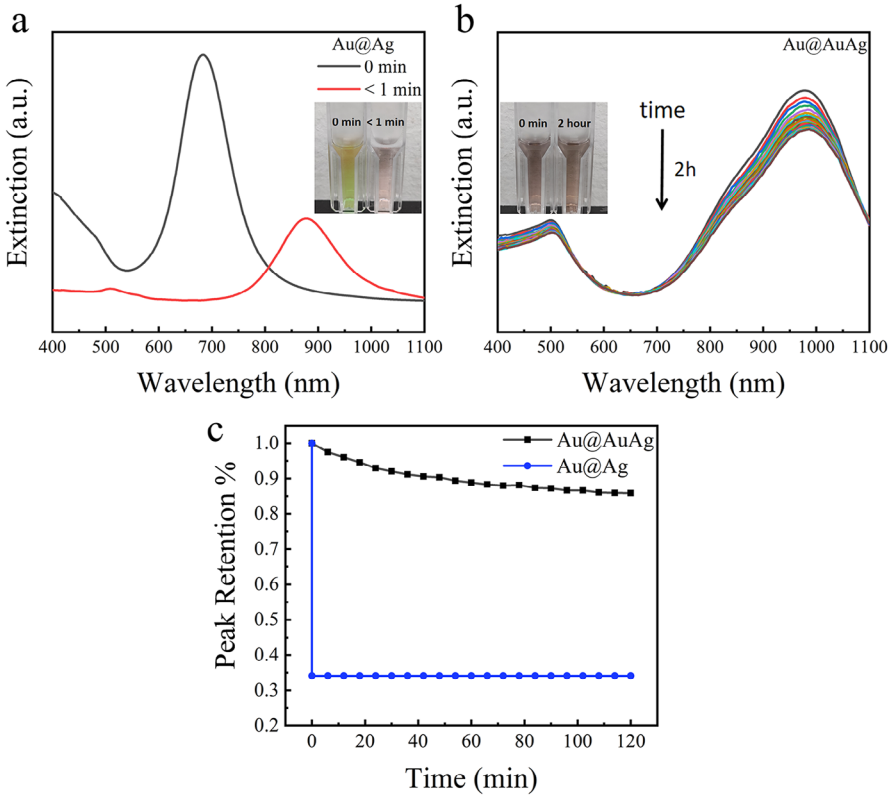

Figure 5. The chemical stability of Au@Ag and Au@AuAg in hydrogen peroxide and ammonia aqueous solution. a) UV–vis–NIR spectra of Au@Ag before (black curve) and after (red curve) the reaction. b) UV–vis spectra and solution color of Au@AuAg at 6-min intervals under corrosive conditions, with a total duration of 2 h. Insets in Figure 5a,b show the solution in curvets before and after reaction. c) Time-dependent retention of peak intensity relative to the initial intensity for Au@AuAg (black line) and Au@Ag (blue line).

3. Conclusion

In summary, we present a facile approach to fabricate hollow core-shell Au@AuAg nanostructures using highly monodisperse AuNRs as the core. By adjusting the ratio of gold to silver, as well as the proportion of CTAB to CTAC, the hollow morphology can be precisely tuned. Subsequent studies reveal that the Au@AuAg nanoparticles possess enhanced chemical stability due to their bimetallic alloy shell. The introduction of the hollow layer and the bimetallic composition endows these Au@AuAg nanostructures with higher refractive index sensitivity and superior SERS performance compared to pristine AuNRs. FDTD simulations of the electromagnetic near-field distribution confirm that the SERS hotspots are located at the two sides of the Au nanorod core and the top and bottom vertices, which significantly amplifies the SERS effect. Therefore, these Au@AuAg nanostructures are expected to have a broad applications in biosensing and bioimaging. Additionally, they hold potential for use in imaging, photothermal therapy, catalysis, and light-responsive detection of specific chemicals.

4. Experimental Section

Materials: All chemicals were used as received without further purification. Cetyltrimethylammonium bromide (CTAB, >99.0%), L-ascorbic acid (AA, >99.99%), chloroauric acid ($HAuCl_4$), hydrochloric acid (HCl, 37.0 wt.% in water), and glycine ($C_2H_5NO_2$, 99.5%) were purchased from Macklin. Cetyltrimethylammonium chloride (CTAC, >99.0%), sodium borohydride ($NaBH_4$, 98%), sodium oleate (NaOL, >99.8%), and silver nitrate ($AgNO_3$, >99.8%) were obtained from Aladdin. Sodium hydroxide (NaOH) was acquired from Hangzhou Gaojing Fine Chemical Co., Ltd., China. Ultrapure water (Millipore Milli-Q grade) with a resistivity of 18.2 MΩ was used in all of the experiments. All glassware were cleaned with freshly prepared aqua regia (HCl/HNO_3 in 3:1 volume ratio), rinsed with large amounts of water, and dried at 60 °C before usage.

Synthesis of Gold Nanorods (AuNRs): AuNRs were synthesized using a seed-mediated growth method previously reported by Ye et al.[41] Preparation of seed solution: Under vigorous stirring (1200 rpm), a freshly prepared ice-cold $NaBH_4$ solution (0.6 mL, 0.01 M) was added to a mixed solution containing $HAuCl_4$ (10 mL, 0.01 M) and CTAB (10 mL, 0.1 M). After stirring for 2 min, the seed solution changed from pale yellow to brown and was aged at 30 °C for 30 min.

Preparation of Growth Solution: CTAB (55.5 mL, 0.1 M), NaOL (6 mL, 0.2 M), and $AgNO_3$ (5.4 mL, 0.004 M) were successively added to 69.705 mL of H_2O. The mixture was allowed to stand at 30 °C for 15 min. Subsequently, $HAuCl_4$ (7.5 mL, 0.01 M) was added, and the solution was reacted under rapid stirring (700 rpm) for 90 min, changing from pale yellow to colorless. Then, HCl (5.4 mL, 1 M) was added, and the solution was stirred rapidly (700 rpm) for 15 min. After 15 min, AA (0.375 mL, 0.064 M) was added to the solution under vigorous stirring (1200 rpm). After 30 s of reaction, 0.12 mL of the seed solution was added to the growth solution. Finally, the resulting mixture was stirred for 30 s and allowed to stand at 30 °C for 12 h to facilitate the growth of AuNRs.

Synthesis of Au@AuAg Hollow Shell Nanostructures: The as-prepared AuNRs solution possessed a volume of roughly 150 mL. To purify the AuNRs, centrifugation was conducted twice at a rotational speed of

10 000 rpm for a duration of 20 min, followed by the removal of the supernatant. The resultant solution, which was concentrated by a factor of ten, was stored as a stock solution in a 10 mM CTAB medium. The concentrated AuNRs solution was then diluted tenfold with a 0.1 M CTAC solution to obtain an original concentration gold rod solution (the final concentration of CTAC in the reaction solution being ≈ 0.05 M). A volume of 5 mL of the purified and diluted gold rod solution was taken, and $C_2H_5NO_2$ (5 mL, 0.2 M) and NaOH (0.03 mL, 2 M) were separately introduced into it. The solution was placed in an environment maintained at 29 °C and stirred at a speed of 400 rpm for 10 min to attain a stable pH value of 8.5. After a lapse of 10 min, $AgNO_3$ (0.525 mL, 0.004 M), $HAuCl_4$ (0.09 mL, 0.01 M), and AA (0.2 mL, 0.1 M) were added in sequence to the solution under intense agitation (1200 rpm), and the reaction was allowed to proceed for 30 s. Following the 30 s reaction, it could be observed that the solution underwent a rapid color change from light brown to transparent black. Ultimately, the obtained mixture was left to stand undisturbed at 29 °C for a period of one day to facilitate the growth process.

Refractive Index Sensitivity Measurement: Water-glycerol mixtures were used with different volume ratios to adjust the refractive index of the medium surrounding the nanostructures. The refractive indices of pure water and glycerol are 1.3334 and 1.4746, respectively. The volume percentage of glycerol in the liquid mixtures was varied from 0% to 73.63% in steps of 8.18%. Mixtures with glycerol volume percentages ranging from 0% to 90% were prepared. A 200 µL aliquot of the prepared AuNRs and Au@AuAg solutions was added to 900 µL of the water-glycerol mixtures with different ratios, and the extinction spectra of the resulting dispersions were measured. Plasmonic shift curves relative to the refractive index were plotted, and the refractive index sensitivity was determined by linear fitting.

Preparation of SERS Substrates: Au@AuAg and AuNRs solutions of identical concentration were ultrasonicated for 2 min to ensure particle dispersion. Silicon wafers, used as substrates, were first cleaned by ultrasonication in acetone, followed by two rounds of ethanol cleaning. Aliquots of the sonicated Au@AuAg and AuNRs solutions were then deposited onto the cleaned silicon wafers in equal volumes and dried in an oven. After complete drying, a 10^{-5} M dye solution was drop-cast onto both samples in equal amounts, followed by secondary drying to fabricate the SERS substrates.

FDTD Simulations: Finite-difference time-domain (FDTD) is a method for solving Maxwell's equations on a discretized spatial grid in complex geometric structures. FDTD simulations were performed using commercial software (Ansys Lumerical FDTD). A total-field scattered-field source was employed to simulate the interaction of a propagating plane wave with wavelengths ranging from 300 to 1100 nm with the nanostructures. A 3D non-uniform grid was employed, and grid sizes of 0.5 and 0.2 nm were selected to calculate the spectra and electric field distributions of the nanostructures, respectively. For sizing, the average dimensions were determined by TEM. The dielectric function of Au was obtained by fitting points from Palik's data,[53] while the dielectric function of Ag was taken from the data reported by Rakic et al.[54] Based on the Maxwell–Garnett equation, the effective dielectric function of the AuAg alloy was calculated using the effective medium approximation (EMA):[55]

$$\frac{\varepsilon_{\text{eff}} - \varepsilon_{\text{Ag}}}{\varepsilon_{\text{eff}} + \varepsilon_{\text{Ag}}} = \text{P}\frac{\varepsilon_{\text{Au}} - \varepsilon_{\text{Ag}}}{\varepsilon_{\text{Au}} + \varepsilon_{\text{Ag}}} \tag{3}$$

Thus, the effective dielectric functions of AuAg alloy are given by:

$$\varepsilon_{\text{eff}} = \varepsilon_{\text{Ag}} \frac{2\text{P}\left(\varepsilon_{\text{Au}} - \varepsilon_{\text{Ag}}\right) + \varepsilon_{\text{Au}} + 2\varepsilon_{\text{Ag}}}{2\varepsilon_{\text{Ag}} + \varepsilon_{\text{Au}} - \left(\varepsilon_{\text{Au}} - \varepsilon_{\text{Ag}}\right)} \tag{4}$$

Among them, where ϵ_{Au}, ϵ_{Ag}, and ϵ_{eff} are the dielectric functions of Au, Ag, and the composite system (AuAg alloy), respectively. *P* is the proportion of Au in the AuAg alloy that could be obtained from the EDS mapping. After calculating ϵ_{eff}, it was imported into the FDTD software. The real and imaginary parts of ϵ_{eff} are plotted in Figure S10 (Supporting Information).

Corrosion Experiment: The stability of Au@Ag and Au@AuAg samples was comparatively investigated. The Au@Ag nanorods were selected from a series of samples with varying gold-to-silver ratios. For the experiment, 50 µL of H_2O_2 (30%), 50 µL of ammonia solution (28% concentration), 450 µL of water were added to 500 µL of Au@AuAg. A spectrometer was then used to measure the extinction spectra of both samples at 6-min intervals over 2 h. Au@Ag was also used in the corrosion test as a control experiment.

Characterization: Optical extinction spectra were recorded using a UV-1900i spectrophotometer (Shimadzu, Japan) with a 10 mm optical path length. Transmission electron microscopy (TEM) images were acquired on an HT-7700 microscope (Hitachi, Japan) operating at 100 kV. High-resolution transmission electron microscopy (HRTEM) images and energy-dispersive spectroscopy (EDS) analysis were performed on a Talos F200S microscope equipped with a 200 kV acceleration voltage. Surface-enhanced Raman scattering (SERS) measurements were conducted using a LabRAM HR Evolution instrument with a 633 nm laser wavelength and 1% power setting. The particle sizes of the nanoparticles were determined from TEM images using ImageJ software.

Supporting Information

Supporting Information is available from the Wiley Online Library or from the author.

Acknowledgements

The authors thank Sudan Shen for her assistance in TEM at State Key Laboratory of Chemical Engineering (Zhejiang University). T.S.D. acknowledges financial support from Zhejiang Provincial Natural Science Foundation (Grant: LY24F050008) and National Natural Science Foundation of China (NSFC, Grant: 61905056). This work was also supported in part by Shanghai Industrial Collaborative Innovation Project (Grant: HCXBCY-2024-051).

Conflict of Interest

The authors declare no conflict of interest.

Data Availability Statement

The data that support the findings of this study are available from the corresponding author upon reasonable request.

Keywords

core-shell structure, gold nanorods, hollow structure, refractive index sensitivity, surface-enhanced Raman scattering

Received: June 20, 2025
Revised: August 8, 2025
Published online: August 28, 2025

[1] E. Petryayeva, U. J. Krull, *Anal. Chim. Acta* **2011**, *706*, 8.
[2] L. M. Liz-Marzán, *Langmuir* **2006**, *22*, 32.
[3] P. Zijlstra, M. Orrit, *Rep. Prog. Phys.* **2011**, *74*, 106401.
[4] L. L. Xu, Q. Q. Cui, Y. Tian, A. X. Jiao, M. Y. Zhang, S. Li, H. S. Li, M. Chen, *Appl. Surf. Sci.* **2021**, *545*, 149054.

[5] E. J. Zhang, T. S. Deng, Y. C. Cheng, L. Y. Liu, J. F. Gao, J. H. Wen, X. Y. Zhao, J. Liu, *ACS Appl. Nano Mater.* **2024**, *7*, 14596.
[6] X. D. Zhang, D. D. Gao, B. C. Zhu, B. Cheng, J. G. Yu, H. G. Yu, *Nat. Commun.* **2024**, *15*, 3212.
[7] J. R. Mejía-Salazar, O. N. Oliveira, *Chem. Rev.* **2018**, *118*, 10617.
[8] N. Zhou, V. López-Puente, Q. Wang, L. Polavarapu, I. Pastoriza-Santos, Q. H. Xu, *RSC Adv.* **2015**, *5*, 29076.
[9] C. Burda, X. B. Chen, R. Narayanan, M. A. El-Sayed, *Chem. Rev.* **2005**, *105*, 1025.
[10] Y. N. Xia, N. J. Halas, *MRS Bull.* **2005**, *30*, 338.
[11] C. J. Orendorff, T. K. Sau, C. J. Murphy, *Small* **2006**, *2*, 636.
[12] J. Zhai, X. Tao, Y. A. Pu, X. F. Zeng, J. F. Chen, *Appl. Surf. Sci.* **2010**, *257*, 393.
[13] M. B. Gawande, A. Goswami, T. Asefa, H. Z. Guo, A. V. Biradar, D. L. Peng, R. Zboril, R. S. Varma, *Chem. Soc. Rev.* **2015**, *44*, 7540.
[14] J. F. Li, Y. J. Zhang, S. Y. Ding, R. Panneerselvam, Z. Q. Tian, *Chem. Rev.* **2017**, *117*, 5002.
[15] C. Sprodowski, K. Morgenstern, *Nanoscale* **2019**, *11*, 10314.
[16] W. R. Zhao, J. L. Gu, L. X. Zhang, H. R. Chen, J. L. Shi, *J. Am. Chem. Soc.* **2005**, *127*, 8916.
[17] J. Kim, H. S. Kim, N. Lee, T. Kim, H. Kim, T. Yu, I. C. Song, W. K. Moon, T. Hyeon, *Angew. Chem., Int. Ed.* **2008**, *47*, 8438.
[18] Q. Zhang, T.-S. Deng, Y.-Q. Dou, M.-Z. Wei, S. Li, J. Liu, Z. Cheng, *ACS Appl. Nano Mater.* **2022**, *5*, 17048.
[19] S. Jiang, Y. H. Zhang, Y. Y. Wang, Y. R. Zhang, Y. Chen, J. K. Yang, Y. S. Chang, E. Escobedo, J. Y. Gong, *J. Mater. Chem. A* **2025**, *13*, 7503.
[20] J. Langer, D. J. de Aberasturi, J. Aizpurua, R. A. Alvarez-Puebla, B. Auguie, J. J. Baumberg, G. C. Bazan, S. E. J. Bell, A. Boisen, A. G. Brolo, J. Choo, D. Cialla-May, V. Deckert, L. Fabris, K. Faulds, F. J. G. de Abajo, R. Goodacre, D. Graham, A. J. Haes, C. L. Haynes, C. Huck, T. Itoh, M. Ka, J. Kneipp, N. A. Kotov, H. Kuang, E. C. Le Ru, H. K. Lee, J. F. Li, X. Y. Ling, et al., *ACS Nano* **2020**, *14*, 28.
[21] K. A. Willets, R. P. Van Duyne, *Annu. Rev. Phys. Chem.* **2007**, *58*, 267.
[22] S. Thota, S. T. Chen, J. Zhao, *Chem. Commun.* **2016**, *52*, 5593.
[23] A. Wittstock, J. Biener, M. Bäumer, *Phys. Chem. Chem. Phys.* **2010**, *12*, 12919.
[24] A. M. El-Toni, M. A. Habila, J. P. Labis, Z. A. Alothman, M. Alhoshan, A. A. Elzatahry, F. Zhang, *Nanoscale* **2016**, *8*, 2510.
[25] B. Zhao, X. Q. Guo, W. Y. Zhao, J. S. Deng, B. B. Fan, G. Shao, Z. Y. Bai, R. Zhang, *Nano Res.* **2017**, *10*, 331.
[26] V. Thambi, A. R. S. Gautam, S. Khatua, *Nanoscale Adv* **2020**, *2*, 4841.
[27] X. W. Lou, L. A. Archer, Z. C. Yang, *Adv. Mater.* **2008**, *20*, 3987.
[28] J. Liu, S. Z. Qiao, Q. H. Hu, G. Q. Lu, *Small* **2011**, *7*, 425.
[29] Y. Zhao, L. Jiang, *Adv. Mater.* **2009**, *21*, 3621.
[30] G. Q. Fang, X. Lin, J. L. Wu, W. Xu, W. Hasi, B. Dong, *Small* **2025**, *21*, 2408670.
[31] M. Sevilla, P. Valle-Vigón, A. B. Fuertes, *Adv. Funct. Mater.* **2011**, *21*, 2781.
[32] Y. S. Li, J. L. Shi, *Adv. Mater.* **2014**, *26*, 3176.
[33] J. Liu, S. Z. Qiao, S. B. Hartono, G. Q. Lu, *Angew. Chem., Int. Ed.* **2010**, *49*, 4981.
[34] L. Zhang, S. Z. Qiao, Y. G. Jin, Z. G. Chen, H. C. Gu, G. Q. Lu, *Adv. Mater.* **2008**, *20*, 805.
[35] S. N. Shmakov, Y. Jia, E. Pinkhassik, *Chem. Mater.* **2014**, *26*, 1126.
[36] J. Han, M. G. Wang, R. Chen, N. Han, R. Guo, *Chem. Commun.* **2014**, *50*, 8295.
[37] H. Y. Gao, G. Wang, Y. Luan, K. Chaikittikul, X. W. Zhang, M. Yang, W. J. Dong, Z. Shi, *CrystEngComm* **2014**, *16*, 2520.
[38] X. B. Wang, Y. Y. Wang, L. Yang, K. Wang, X. D. Lou, B. B. Cai, *J. Power Sources* **2014**, *262*, 72.
[39] J. Y. Jung, D. G. Kim, I. Jang, N. D. Kim, S. J. Yoo, P. Kim, *J. Ind. Eng. Chem.* **2022**, *111*, 300.
[40] J. Zheng, X. Cheng, H. Zhang, X. Bai, R. Ai, L. Shao, J. Wang, *Chem. Rev.* **2021**, *121*, 13342.
[41] X. Ye, C. Zheng, J. Chen, Y. Gao, C. B. Murray, *Nano Lett.* **2013**, *13*, 765.
[42] V. Thambi, A. Kar, P. Ghosh, D. Paital, A. R. S. Gautam, S. Khatua, *ACS Omega* **2019**, *4*, 13733.
[43] T. Bai, J. Sun, R. Che, L. Xu, C. Yin, Z. Guo, N. Gu, *ACS Appl. Mater. Interfaces* **2014**, *6*, 3331.
[44] Y. F. Huang, K. M. Huang, H. T. Chang, *J. Colloid Interface Sci.* **2006**, *301*, 145.
[45] S. Fateixa, H. I. S. Nogueira, T. Trindade, *ACS Omega* **2018**, *3*, 4331.
[46] R. Mandavkar, S. Lin, S. Pandit, R. Kulkarni, S. Burse, M. A. Habib, S. Kunwar, J. Lee, *Surf. Interfaces* **2022**, *33*, 102175.
[47] C. M. Ruan, W. Wang, B. H. Gu, *J. Raman Spectrosc.* **2007**, *38*, 568.
[48] Y. Lei, P. Du, J. X. Hu, Z. Ouyang, Z. C. Jiang, Y. Y. Lin, Y. C. Wu, *J. Mater. Sci. Mater.* **2021**, *32*, 956.
[49] M. Zannotti, A. Rossi, R. Giovannetti, *Coatings* **2020**, *10*, 288.
[50] J. E. S. van der Hoeven, H. Gurunarayanan, M. Bransen, D. A. M. de Winter, P. E. de Jongh, A. van Blaaderen, *Adv. Funct. Mater.* **2022**, *32*, 2200148.
[51] A. D. McFarland, M. A. Young, J. A. Dieringer, R. P. Van Duyne, *J. Phys. Chem. B* **2005**, *109*, 11279.
[52] C. Gao, Y. Hu, M. Wang, M. Chi, Y. Yin, *J. Am. Chem. Soc.* **2014**, *136*, 7474.
[53] E. E. D. Palik, *Handbook of Optical Constants of Solids*, Academic Press, Cambridge, Massachusetts, USA **1991**.
[54] A. D. Rakic, A. B. Djurisic, J. M. Elazar, M. L. Majewski, *Appl. Opt.* **1998**, *37*, 5271.
[55] J. C. M. Garnet, *Philos. Trans. R. Soc. A* **1904**, *203*, 385.

Supporting Information

Synthesis of Gold Nanorod@AuAg Hollow Shell Nanostructures with Enhanced Refractive Index Sensitivity and SERS Activity

Zhen-Ming Shen[1], Jie Liu[1,], Kun-Peng Wang[1], Xi-Hao Zhang[1], Lan Chen[1], Zhigang Zhou[1], and Tian-Song Deng[1,2,*]*

[1]School of Electronics and Information Engineering, Hangzhou Dianzi University, Hangzhou 310018, China

[2]Key Laboratory of Micro-nano Sensing and IoT of Wenzhou, Wenzhou Institute of Hangzhou Dianzi University, Wenzhou, 325038, China

[*]Corresponding author. E-mail: dengts@pku.edu.cn, liujie4209@hdu.edu.cn

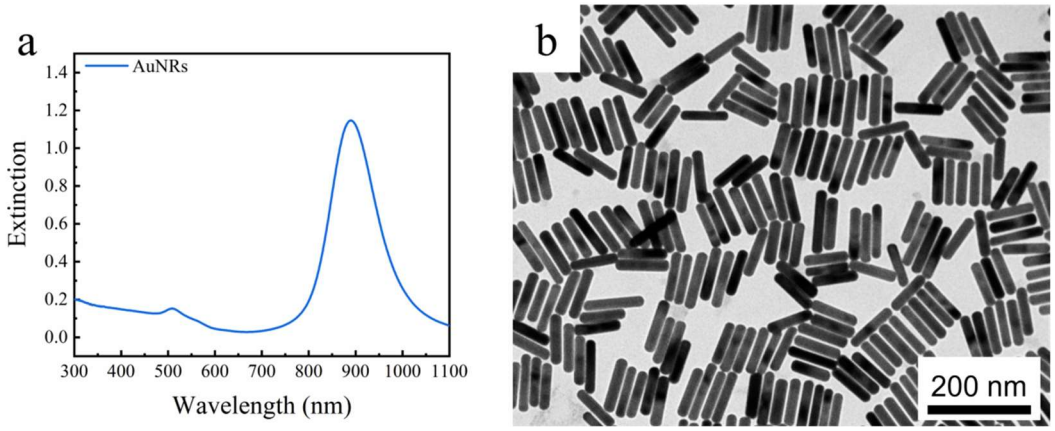

Figure S1. UV-vis-NIR spectrum (a) and TEM image (b) of the AuNRs. The gold nanorod samples have a length of 90.8 ± 6.8 nm, and a width of 18.4 ± 2.1 nm.

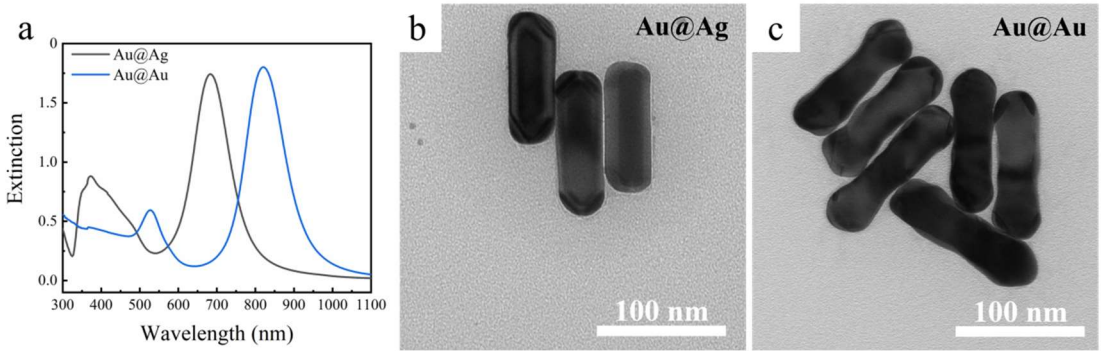

Figure S2. UV-vis-NIR spectra and TEM images of the nanoparticles. (a) UV-vis-NIR spectra of Au@Ag core-shell nanorods (black curve) and Au@Au nanorods (blue curve). The TEM images show (b) Au@Ag core-shell nanorods and (c) Au@Au nanorods. The Au@Ag core-shell samples exhibit a core-shell structure with a near-rectangular shape, with a length of 116.5 ± 8.1 nm and a width of 38.5 ± 2.0 nm; while the Au@Au nanorod samples have a length of 113.2 ± 6.1 nm and a width of 32.5 ± 2.1 nm.

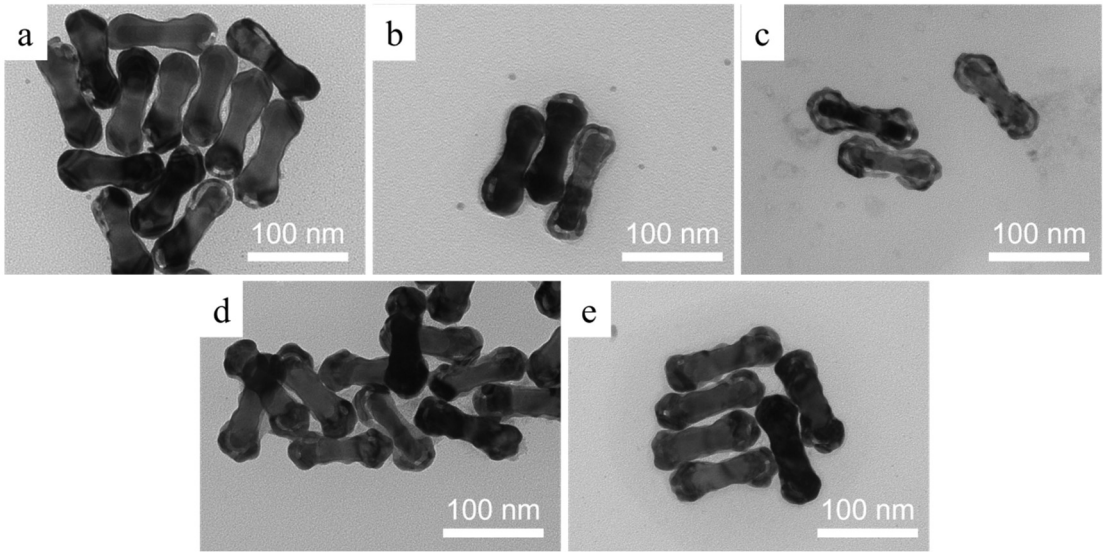

Figure S3. TEM images of Au@AuAg nanostructures at different gold-to-silver ratios: (a) Au:(Au+Ag) = 10%, (b) Au:(Au+Ag) = 20%, (c) Au:(Au+Ag) = 30%, (d) Au:(Au+Ag) = 40%, and (e) Au:(Au+Ag) = 50%.

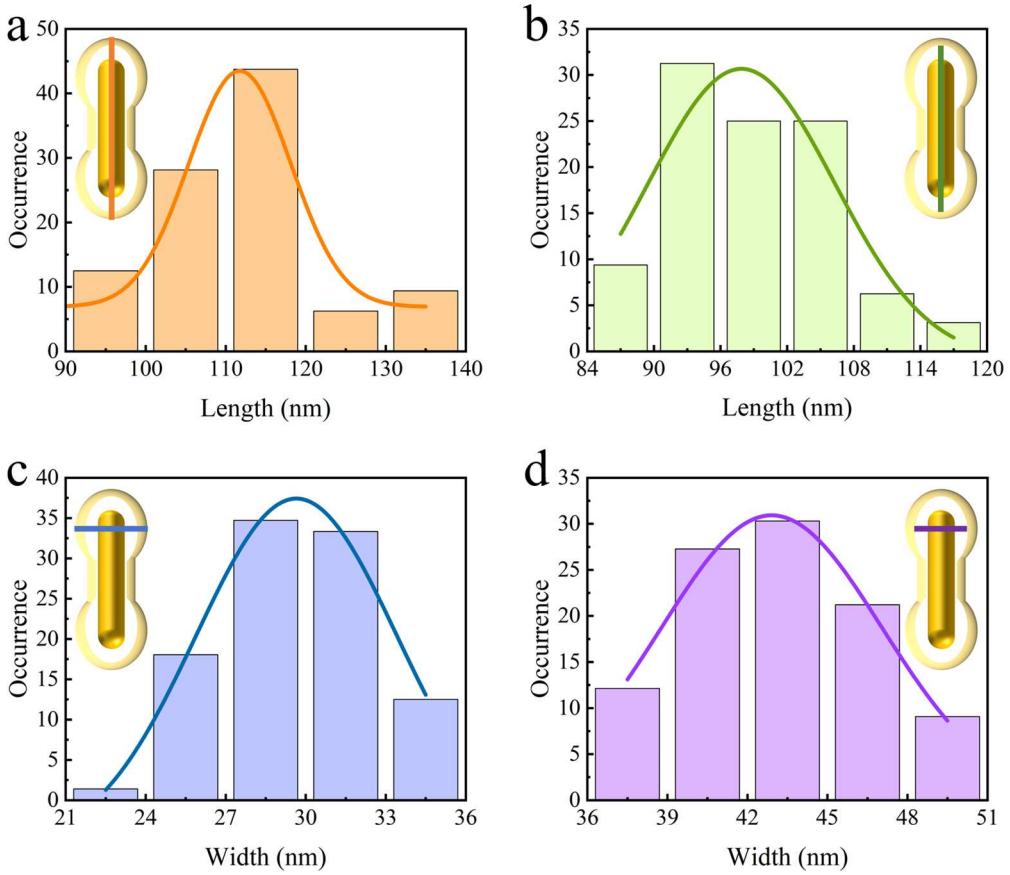

Figure S4. Length and width histogram distributions of Au@AuAg nanostructures and their hollow interiors: Au@AuAg nanostructures: (a) Average length = 113.2 ± 9.1 nm, (c) Average width = 43.2 ± 3.3 nm. Hollow interiors of Au@AuAg: (b) Average length = 98.6 ± 7.1 nm, (d) Average width = 29.6 ± 2.9 nm.

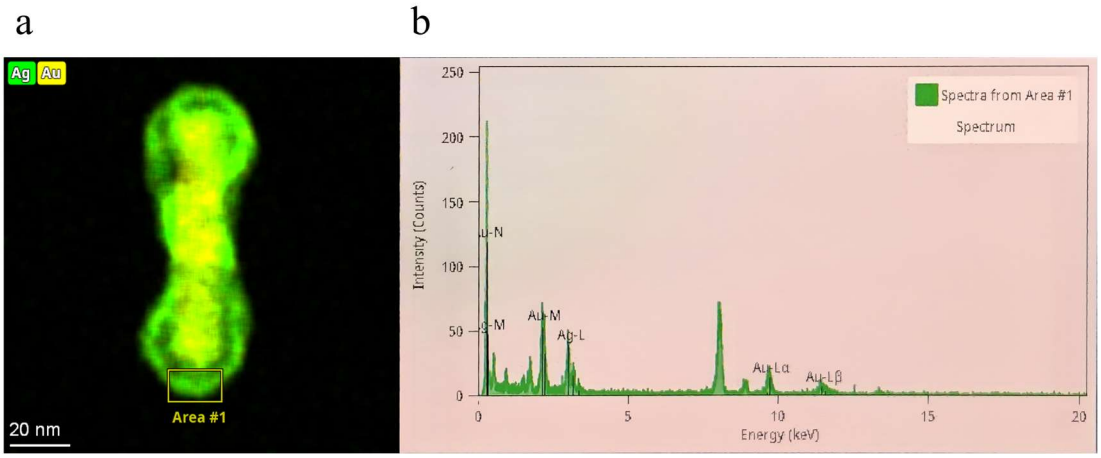

Figure S5. Region (a) and net counts (b) of Au and Ag content in the hollow shell detected by EDS.

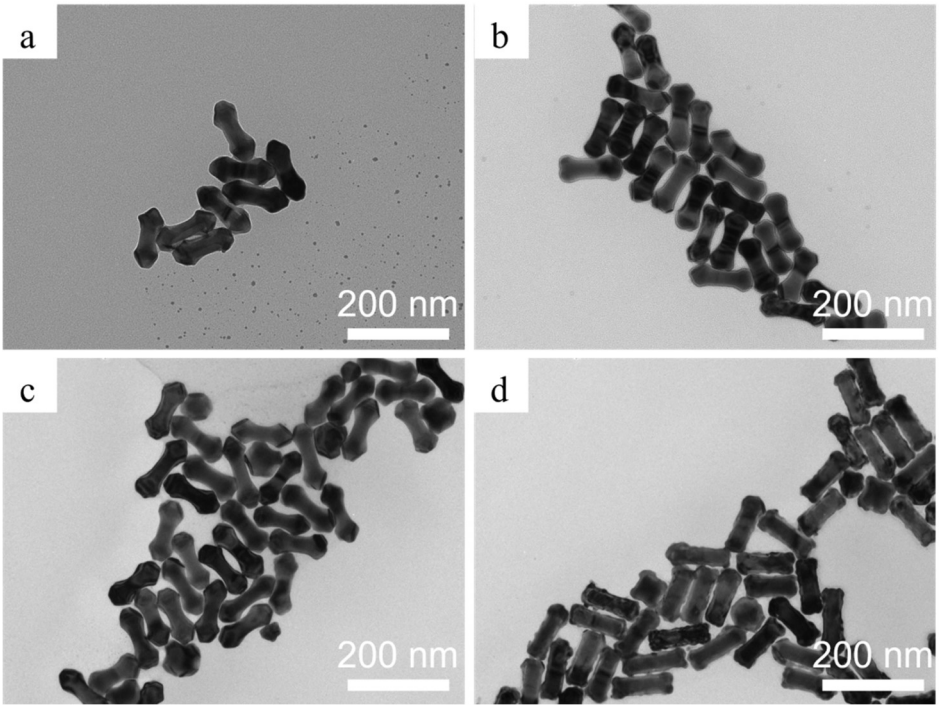

Figure S6. TEM images of Au@AuAg nanostructures at different CTAC/(CTAB+CTAC) ratios: (a) 75%, (b) 50%, (c) 25%, and (d) 0%.

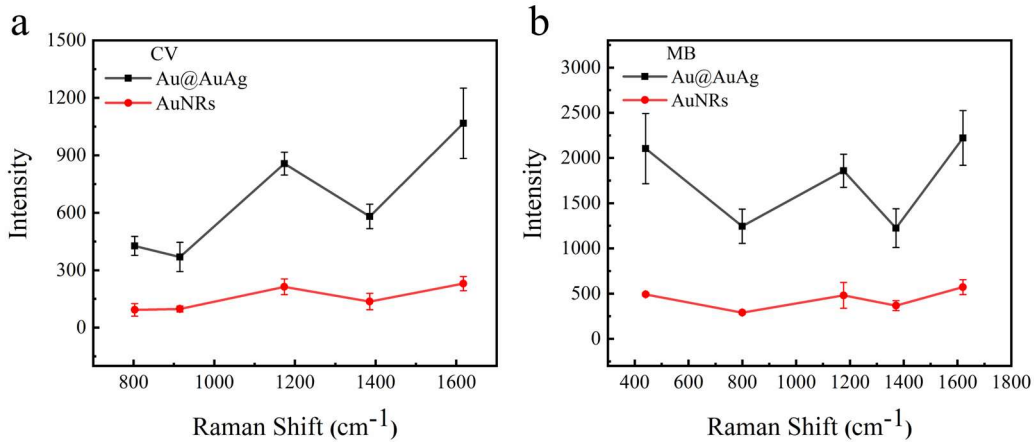

Figure S7. Measured SERS intensity of the AuNRs and Au@AuAg (a) characteristic band of CV at 802, 914, 1173, 1385, and 1617 cm^{-1}. (b) characteristic band of MB at 440, 799, 1176, 1371, and 1620 cm^{-1}.

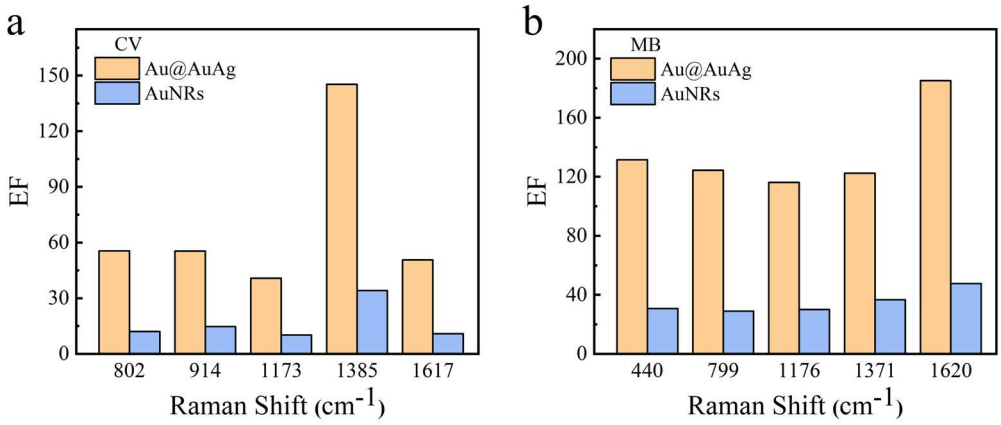

Figure S8. The SERS enhancement factors of the AuNRs and Au@AuAg (a) characteristic band of CV at 802, 914, 1173, 1385, and 1617 cm^{-1}. (b) characteristic band of MB at 440, 799, 1176, 1371, and 1620 cm^{-1}.

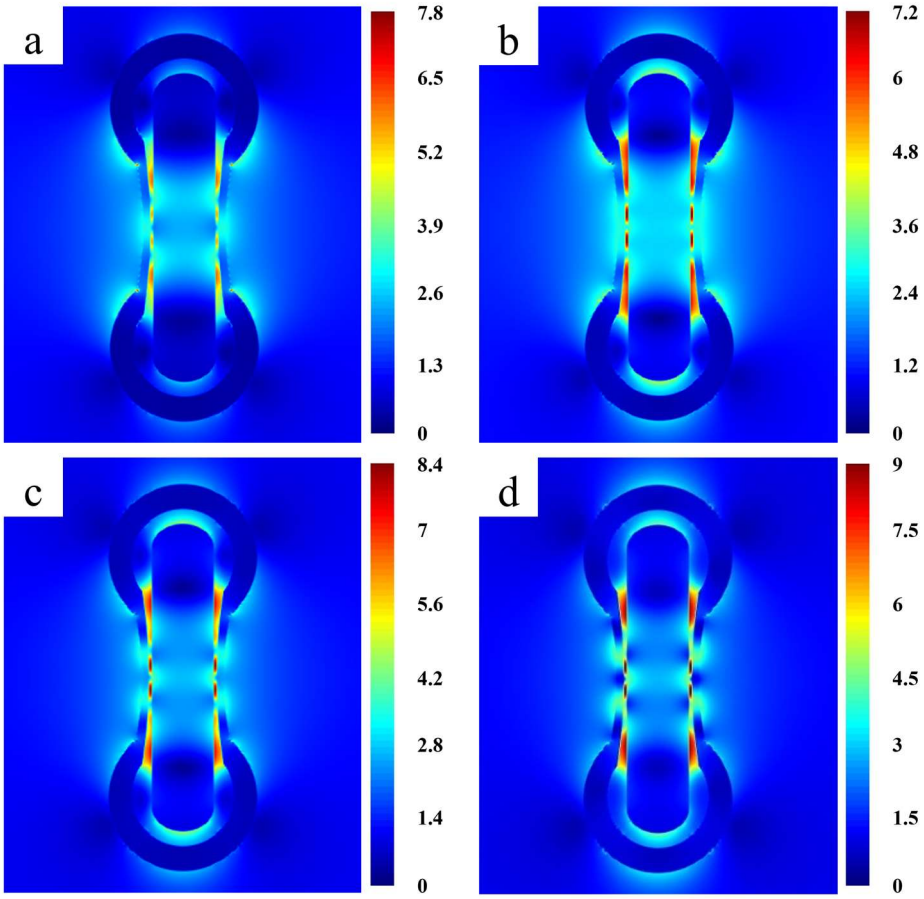

Figure S9. FDTD simulations of electric field distributions with different ratios of Au:(Au+Ag) in the shell of Au@AuAg structures: (a) 0%, (b) 50%, (c) 75%, and (d) 100%. The enhancement effect of the electric field first decreases and then increases with increasing gold content in the Au-Ag alloy.

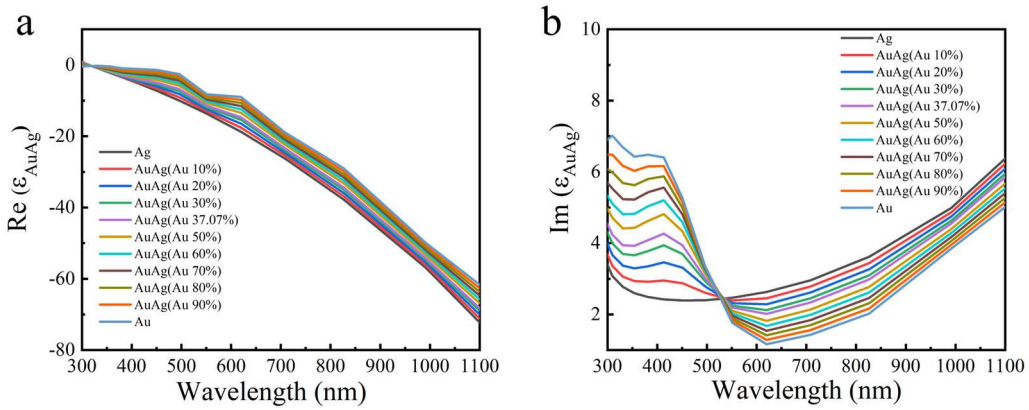

Figure S10. Dielectric function of the AuAg alloy with different Au/(Au+Ag) ratio. (a) the real part, and (b) the imaginary part.